https://doi.org/10.5194/egusphere-2025-2612
Preprint. Discussion started: 7 August 2025

Non-Invasive Assessment of Aircraft Engine Particulate Matter Emissions with Lidar

Romain Ceolato [1,*], Andrés Bedoya-Velásquez [1], Gerald Lemineur [1], Pierrick Loyers [2], Charles Renard [2], Katharina Seeliger [2], Louise Ganeau [3], Alaric Vandestoc [3], Ismael Ortega [3], Mark Johnson [4], and David Delhaye [5]

[1]ONERA, Université de Toulouse, Toulouse, France
[2]Airbus Operations SAS, Toulouse, France
[3]ONERA, Paris-Saclay University, F-91123 Palaiseau, France
[4]Rolls-Royce plc, Derby, United Kingdom
[5]DGAC French Civil Aviation Authority, Paris, France

Correspondence: Romain Ceolato (Romain.Ceolato@onera.fr)

Abstract. Particulate matter (PM) emitted by aircraft engines primarily consists of soot particles formed through incomplete fuel combustion, which can act as ice nuclei in the formation of contrails and contribute to poor air quality around airports. A novel technique is introduced to investigate aircraft engine PM emissions using a short-range elastic backscattering lidar. This approach was validated through trials conducted at the Airbus Bikini test site using the compact and field-deployable Colibri Aerosol Lidar (CAL) sensor. This instrument enables rapid, non-invasive, and remote measurement of volume backscatter profiles, which can be converted into PM mass and number concentrations without the need to sample particles from the aircraft exhaust. Our findings demonstrate the feasibility and potential of using a short-range elastic backscattering lidar for remote assessment of aircraft PM emissions across various engine thrust levels.

1 Introduction

Quantifying non-CO2 emissions from aircraft engines, particularly non-volatile particulate matter (nvPM) or soot particles, have become a critical focus in aviation environmental research (Lee et al., 2023). These emissions impact local air quality around airports and contribute to the formation of contrails and contrail-induced cirrus clouds, which may influence the global Earth's radiative balance by altering light absorption and scattering in the stratosphere (Yu et al., 2024; Klöwer et al., 2021). Regulatory standards, such as those established by the International Civil Aviation Organization (ICAO, 2017), are also driving industry efforts to reduce PM emissions from aircraft engines including technological advances in engine design, the use of low-sulfur jet fuel, and improved combustion efficiency. The PM emissions at the aircraft turbine engine exit plane consist mainly of nonvolatile Particulate Matter (nvPM), or black carbon soot, while other constituents, such as volatile Particulate Matter (vPM), may be formed downstream as the exhaust plume dilutes and cools in the atmosphere. These vPM are comprised primarily of sulfur and organic compounds and generally do not form until the exhaust plume has sufficiently diluted and cooled in the atmosphere downstream of the engine (Jones and Miake-Lye, 2024). The nvPM are defined as solid particles formed by the combustion process, with diameters typically between 10 nm and 100 nm, and present at the engine exit plane at temperatures

https://doi.org/10.5194/egusphere-2025-2612
Preprint. Discussion started: 7 August 2025

higher than 350 °C (SAE International, 2018, 2019). Therefore, there has been a growing need to monitor nvPM emissions from aircraft to better understand their composition and formation mechanisms, to mitigate their environmental and health effects.

The measurement of nvPM emissions from aircraft engines is challenging due to the complex nature of the exhaust plume, which involves high temperatures, high velocities, and rapid dilution in the atmosphere. Engine certification procedure for measuring nvPM concentrations has evolved recently, going from the measurement of smoke number to the measurement of nvPM number and mass concentration (ICAO, 2017). Certification measurements require sample dilution and long lines (up to 32 meters), leading to significant uncertainties, especially in line loss corrections, and making it hard to estimate engine exit plane values (Durand et al., 2023). Because of these challenges and the need for loss correction methods, new techniques have been developed to measure nvPM emissions from aircraft engines. These techniques include laser or active remote-sensing methods, such as elastic backscatter lidar (EBL), which can provide information about the presence, distribution, and relative concentration of a wide range of atmospheric aerosols, including soot particles.

Recent advancements have brought the use of lidar techniques closer to new applications involving in-situ instruments. In particular, Short-Range Elastic Backscatter Lidar (SR-EBL) techniques have proven to be able to probe the mass and number concentration of black carbon aerosols in the first tens of meters, unlike traditional long-range atmospheric lidars. SR-EBL sensors have demonstrated the ability to provide precise and non-invasive characterization of particulate matter near ground level, in synergy with in-situ instruments for monitoring urban air pollution and traffic-related emissions (Bedoya-Velásquez et al., 2024). These emerging lidar techniques may offer a more dynamic and continuous alternative to conventional in-situ sampling methods for assessing nvPM concentrations, such as aircraft gas engines.

Here, we introduce a novel approach for directly measuring nvPM from an aircraft engine using a short-range aerosol lidar. First, the sensor and associated retrieval methodology are described. Subsequently, measurements are presented to demonstrate the feasibility and potential of this technique for monitoring on-wing engine particulate emissions. Our novel sensor is designed to offer a rapid, precise, and efficient characterization of soot emissions, while overcoming the limitations associated with in situ sensors. The development of this sensor represents a step forward in the monitoring of non-CO2 aircraft emissions, contributing to efforts to mitigate the environmental impact of the aviation sector.

2 Materials and methods

2.1 Principle of measurement

In this section, an overview of the principle of the backscatter lidar-based technique is provided. The principle of operation has been described in further detail in previous work Ceolato and Berg (2021). Briefly, the short-range elastic backscatter lidar (SR-EBL) technique consists in measuring the range-dependent backscattering intensity using the Time-of-Flight (ToF) method to achieve a higher signal-to-noise ratio compared to other optical methods. The raw lidar signal $S(r)$ directly depends on the volume of illuminated particulate matter, located at a distance r from the sensor. It is a common practice to use the

https://doi.org/10.5194/egusphere-2025-2612
Preprint. Discussion started: 7 August 2025

range-corrected signals RCS instead of the lidar signal to remove the range dependence on the signal, such as :

$$\mathrm{RCS(r)} = S(r)r^2 = \mathrm{K_o}(r)U(r) \qquad [\mathrm{V\ m^2}] \tag{1}$$

where $\mathrm{K_o}(r)$ is the lidar constant, directly derived from the radiometric lidar constant, which depends on several parameters such as the laser pulse energy or the sensor gain and sensitivity, and the overlap or geometric function. We note that the lidar calibration constant changes from instrument to instrument because of the variation in laser, optical loss, and sensor response. The elastic lidar equation provides a simple expression of the attenuated backscatter profiles $\mathrm{U}(r)$ under the single-scattering approximation (SSA) Measures (1984); Ceolato and Berg (2021), i.e.

$$\mathrm{U}(r) = \beta(r)T(r) \quad \text{where} \quad T(r) = \exp\left(-2\int_0^r \alpha(r')\,\mathrm{d}r'\right), \tag{2}$$

where $\alpha(r)$ and $\beta(r)$ are the range-dependent *volume* extinction and backscattering coefficients, with units of $[\mathrm{m^{-1}}]$ and $[\mathrm{m^{-1}sr^{-1}}]$, respectively.

For optically thin combustion plumes such as aircraft exhaust plumes, i.e. $T(r) \sim 1$, the volume backscattering coefficient $\beta(r)$ is approximately equal to the attenuated backscattering coefficient $U(r)$. Thus, Eq. 1 becomes,

$$\mathrm{RCS(r)} = \mathrm{K_o}(r)\beta(r) \qquad [\mathrm{V\ m^2}]. \tag{3}$$

All optical instruments, including in-situ and remote sensing techniques, rely on having the appropriate optical model to invert raw electrical signals into useful information. For instance, Laser Induced Incandescence (LII) requires a solid knowledge of soot refractive index to infer absorption efficiency and retrieve mass concentration information. Absorption instruments such as the Single-Particle Soot Photometer (SP2) use the mass-absorption coefficient (MAC) Fengshan Liu and Corbin (2020), while extinction instruments such as the Photoacoustic Extinctiometer (PAX) or the Cavity Attenuated Phase Shift Extinction Monitor (CAPS) use the mass-extinction coefficient (MEC) Smith et al. (2015). Here, SR-EBL relies on the backscattering properties of soot particles. Among these properties, two main parameters are needed to invert the CAL sensor signals into number and mass concentrations: the differential backscattering cross-section $\mathrm{d}C^{\mathrm{bac}}$ and the mass-backscattering coefficient (MBC), respectively. The volume backscattering coefficients can be converted to *equivalent* number and mass concentrations by dividing them by a reference coefficient.

The range-dependent particle number concentration $n_\mathrm{o}(r)$ is directly related to the volume backscattering coefficient,

$$n_\mathrm{o}(r) = \frac{\beta(r)}{\mathrm{d}C^{\mathrm{bac}}} \tag{4}$$

where $\mathrm{d}C^{\mathrm{bac}}$ is the mean differential backscattering cross-section, with units of $[\mathrm{m^2sr^{-1}}]$, defined as,

$$\mathrm{d}C^{\mathrm{bac}} = \overline{\mathrm{d}C^{\mathrm{bac}}} = \int_{R_{\mathrm{min}}}^{R_{\mathrm{max}}} p(R)\mathrm{d}C^{\mathrm{bac}}(R)\,\mathrm{d}R \tag{5}$$

where $p(R)$ is the normalized probability density function (PDF). The soot aerosols are assumed to constitute an isotropic scattering medium consisting of a log-normal ensemble of randomly oriented particles with a mean geometric radius R. The radii

https://doi.org/10.5194/egusphere-2025-2612
Preprint. Discussion started: 7 August 2025

R_{min} and R_{max} in Eq. (5) denote the minimum and maximum geometric mean radii, respectively. The differential backscattering cross section $\mathrm{d}C^{\text{bac}}$ can, in general, be obtained from the Stokes phase matrix Mishchenko et al. (2002).

Similarly, the range-dependent particle mass concentration $m_{\text{o}}(r)$ is directly related to the volume backscattering coefficient,

$$m_{\text{o}}(r) = \frac{\beta(r)}{\text{MBC}} \tag{6}$$

where MBC, with units of $[\text{m}^2\text{g}^{-1}\text{sr}^{-1}]$, is defined as the ratio

$$\text{MBC} = \frac{\mathrm{d}C^{\text{bac}}_{\text{soot}}}{m_{\text{soot}}} = \frac{\mathrm{d}C^{\text{bac}}_{\text{soot}}}{\rho V_{\text{soot}}} \tag{7}$$

where m_{soot} is the mass of a soot particle and ρ is the soot density with units $[\text{kg}\,\text{m}^{-3}]$. This coefficient, also called specific mass backscattering coefficient, is essential to convert lidar signals into mass concentration. It can be seen as the backscattering analogue to the MAC or MEC used by other traditional optical techniques.

Consequently, the retrieval of physical quantities from lidar measurements relies on the use of appropriate optical properties. It is important to acknowledge that the performance of the SR-EBL in measuring particle number and mass concentrations is dependent on the knowledge of the optical properties of particulate matter. This information can be obtained through laboratory calibration or by employing a suitable aerosol optical model. The latter approach is the method of choice in this study based on the state-of-the-art knowledge of aircraft soot particles and will be elaborated upon subsequently.

2.2 Optical model for aircraft engine particulate matter

Modeling backscattering properties is particularly challenging for soot particles, which are highly absorbing and have complex optical properties, and has been investigated in previous studies Kanngiesser and Kahnert (2019); Liu and Mishchenko (2020). Numerical calculations of the radiative properties of soot have been developed using various light-scattering theories: ranging from the Lorenz-Mie theory, which assumes simple spherical shapes, to more advanced approaches such as the T-Matrix and Discrete Dipole Approximation (DDA) methods, which account for more complex morphologies Qin et al. (2024); Ishimoto et al. (2019). These methods offer varying levels of accuracy for applications in atmospheric science, combustion diagnostics, and climate research.

A backscattering model based on the Rayleigh-Debye-Gans for Fractal Aggregates (RDG-FA) is proposed for modeling the lidar parameters of soot particles, accounting for their fractal morphology. This model is a light-scattering approximation for fractal aggregates, based on two assumptions: monomers scatter light independently, and the phase shift across each monomer is negligible. Its accuracy depends on parameters like monomer size, fractal dimension, wavelength, and refractive index, and has been extensively discussed in previous works Sorensen (2001). These assumptions hold for soot particles with small aggregate with small monomers, which are typically found in aircraft particulate matter emissions. Despite its simplicity, RDG-FA shows good agreement with experimental light-scattering data for soot, especially when averaged over random aggregate orientations, and has been recently introduced for lidar inversion. This model was successfully used for retrieving kerosene number and mass concentration from a turbulent small-scale kerosene pool fire Ceolato et al. (2022).

https://doi.org/10.5194/egusphere-2025-2612
Preprint. Discussion started: 7 August 2025

In the following, we will model the aircraft engine particulate matter as soot fractal aggregates Teoh et al. (2019). Such aggregates are considered fractal if they display self-similarity across their size scales, that relates aggregate mass or number of monomers N, and follows the classic *fractal scaling law*,

$$N = k_{\mathrm{o}} \left(\frac{D_{\mathrm{g}}}{D_{\mathrm{m}}} \right)^{D_{\mathrm{f}}}, \tag{8}$$

where the fractal dimension D_{f} characterizes the overall morphology of the aggregates and the fractal prefactor k_{o} represents a degree of compactness of the aggregate. In addition to these morphological parameters, the size of the particles are expressed in terms of the monomer diameter, D_{m}, and the diameter of gyration, D_{g}, which represents the radius of a sphere with the same moment of inertia as an aggregate with N monomers. Here, the proposed values of the soot fractal aggregate model for aircraft particulate matter is based on the following parameters : $D_{\mathrm{f}} = 1.9$, $k_{\mathrm{o}} = 2.3$, $D_{\mathrm{m}} = 20$ nm, and $D_{\mathrm{g}} = 50$ nm. These values are typically obtained from imaging techniques such as transmission electron microscopy (TEM), as reported in the literature Delhaye et al. (2017); Marhaba et al. (2019). Furthermore, the ratio $X_R = D_{\mathrm{m}}/D_{\mathrm{g}} = 0.4$ is consistent with the median value derived from measurements and used to model soot particle Kumal et al. (2020); Yu et al. (2024). However, significant uncertainties remain regarding the nvPM morphological properties of modern engines such as the TXWB-84. This gap highlights the need for further research and comprehensive measurements. The selection of an appropriate complex refractive index for soot remains debated due to the complex and interrelated uncertainties involved Digby et al. (2024). The recently recommended value of $m = 1.95 + 0.96i$ for freshly emitted black carbon N. Moteki and Adachi (2023) is used here and corresponds to a low organic carbon to total carbon ratio (OC/TC), as reported for most aircraft engine thrusts Marhaba et al. (2019); U. Trivanovic and Pratsinis (2022). Another key parameter is the effective mass density for particulate matter, commonly assumed to be $\rho = 1000$, $\mathrm{kg\,m^{-3}}$ in aircraft particulate studies ICAO (2017); Durdina et al. (2014). More complex and size-resolved effective density models have been developed, but this value has been shown to give accurate results for a wide range of engine thrusts Durdina et al. (2014).

An aerosol-optics model is proposed here based on the Rayleigh-Debye-Gans approximation for Fractal Aggregates (RDG-FA). Here, the differential backscattering cross-section is defined in the backward scattering direction, i.e., for $\theta = \pi$, where θ is the (polar) scattering angle as,

$$\mathrm{d}C^{\mathrm{bac}} = N^2 k^4 R_{\mathrm{m}}^6 F(m) S(q_\pi, R_g, D_{\mathrm{f}}), \tag{9}$$

or using the aggregate volume $V_{\mathrm{agg}} = \frac{4}{3}\pi N R_{\mathrm{m}}^3$:

$$\mathrm{d}C^{\mathrm{bac}} = 9\pi^2 \frac{V_{\mathrm{agg}}^2}{\lambda^4} F(m) S(q_\pi, R_{\mathrm{g}}, D_{\mathrm{f}}), \tag{10}$$

with $q_\pi = q(\theta = \pi, \lambda) = 2k$ defined as the *backscattering wave-vector*. In conventional light-scattering studies, the scattering angle is varied to change q, and thus, probe different length scales (q^{-1}). Note however, that in elastic backscatter lidar applications, where the angle is fixed at $\theta = \pi$, different length scales can still be probed by varying λ. For our lidar sensor, $q_\pi = 0.0236$ $\mathrm{nm^{-1}}$ for a laser emitting at 532 nm.

https://doi.org/10.5194/egusphere-2025-2612
Preprint. Discussion started: 7 August 2025

An important parameter to introduce here is the backscattering structure factor $S(q_\pi, R_\mathrm{g}, D_\mathrm{f})$. This factor describes the backscattered intensity in the RDG-FA approximation and has been widely used to characterize combustion by-products. It is a dimensionless value defined as the square of the Fourier transform of the auto-correlation function, representing an aggregate's structure in reciprocal space, and can be divided into three regimes scattering regimes Sorensen (2001). Several analytical expressions for $S(q)$ are available and can be used to express $S(q_\pi)$. Each have in common that yield the characteristic behavior of the Guinier and power-law regimes described above.

A popular expression is the one proposed by Dobbins and Megaridis **?** as ,

$$S(q_\pi) = \begin{cases} \exp\left(-\dfrac{q_\pi^2 R_\mathrm{g}^2}{3}\right) & \text{if} \quad q_\pi R_\mathrm{g} < \sqrt{\dfrac{3D_\mathrm{f}}{2}}, \\ \left(\dfrac{3D_\mathrm{f}}{2e q_\pi^2 R_\mathrm{g}^2}\right)^{-\frac{D_\mathrm{f}}{2}} & \text{if} \quad q_\pi R_\mathrm{g} > \sqrt{\dfrac{3D_\mathrm{f}}{2}}, \end{cases} \tag{11}$$

where $e = 2.718$. In the following, due to the small size of the particulate matter emitted by the aircraft engine such as $q_\pi R_\mathrm{g} < \sqrt{\frac{3D_\mathrm{f}}{2}}$, a simple expression of the differential backscattering cross-section can be used as :

$$\mathrm{d}C^\mathrm{bac} = 9\pi^2 \frac{V_\mathrm{agg}^2}{\lambda^4} F(m) \exp\left(-\frac{q_\pi^2 R_\mathrm{g}^2}{3}\right), \tag{12}$$

2.3 Colibri Aerosol Lidar (CAL) sensor

A novel sensor, named Colibri Aerosol Lidar (CAL), has been developed for measuring nvPM concentrations in real-time with high accuracy, without sampling, directly from an aircraft engine exhaust. Different versions of the CAL instrument have been developed to address various needs and measurement scenarios Ceolato et al. (2022, 2020b). The CAL-210 is a compact and lightweight forward-looking short-range elastic backscatter lidar (SR-EBL) with a bi-static and multi-axial architecture for remote measurements of aerosols with a range resolution of 10 cm and a time resolution of 1 ms. The emitter unit consists of a compact, air-cooled Nd:YAG laser that emits ns pulses with a pulse energy of 25 mJ, wavelength of $\lambda = 532.8$ nm, 20 Hz, and a beam divergence of 0.5 mrad. A pair of lenses expands and collimates the laser beam before directing it toward the particulate matter, here the aircraft engine exhaust plume. The receiver unit, which features a Cassegrain telescope with a 90 mm effective diameter and a field-stop (FS) to control the field of view, collects the backscattered light. Then, a collection of optical elements, including achromatic doublet (AD) lenses, a neutral-band filter (NBF), and an interference filter (IF), is placed on a translation stage to allow fine adjustment of the focal plane. This feature is crucial as it resolves focusing problems encountered for short ranges. The bi-static angle, i.e. the angle subtended between the transmitter and receiver units, is another essential feature for short-range measurements as it enables full control of the overlap function. Subsequently, the sensing unit incorporates an ultrafast photomultiplier tube (PMT). The signal from the PMT is digitized by a 12-bit analogue-to-digital converter (ADC) at a sampling rate of 1 GS/s, then processed by a field-programmable gate array (FPGA) to extract the distance-resolved backscatter

https://doi.org/10.5194/egusphere-2025-2612
Preprint. Discussion started: 7 August 2025

signal. The data is then transmitted to a computer for analysis and processing to determine the range-resolved backscatter signal using the Time-of-Flight (ToF) principle, which depend upon the number and mass concentration, n_o and m_o respectively.

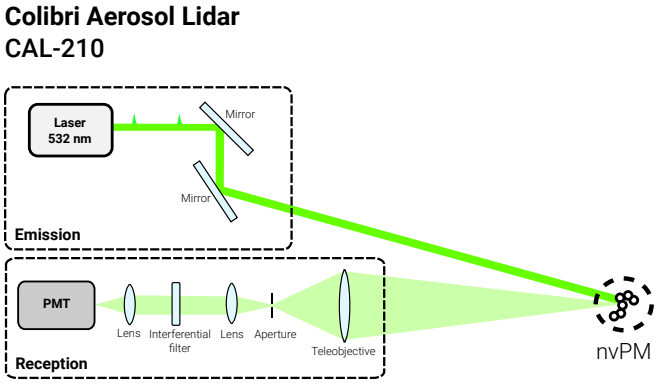

Laser	Wavelength	532 nm
	Pulse duration	6 ns
	Pulse repetition rate	1.0 kHz
	Pulse energy	20 mJ
	Beam divergence	0.5 mrad
	Beam diameter	1 mm
	Bi-static angle	1–5 mrad
Receiver	Type	Cassegrain
	Effective diameter	90 mm
	Focal length	500 mm
Sensor	Type	Hamamatsu PMT
	Bandwidth	1.0 GHz
	Active area	0.2 mm^2

Figure 1. Optical diagram and specifications of the CAL-210 sensor. A Nd:YaG laser along with a collimator emits a laser beam in the direction of the aerosol plume. The backscattered light is collected by a compact Cassegrain telescope then relayed by another achromatic lens to the PMT.

The salient advantages of the SR-EBL technique, which is employed by the CAL sensor, are outlined below. Firstly, it provides a direct measurement of particles, thus obviating the potential errors associated with sampling. Specifically, sampling biases and contamination are two major sources of uncertainties that can significantly impact the accuracy of nvPM measurements. Secondly, by reducing the overlap between the laser and receiver field of view, it leverages aerosol lidar technology to directly measure particles in short-range, close to the aerosol emission source, such as an aircraft engine. This technique thereby bridges the gap between in-situ and remote sensing techniques. In summary, this innovation eliminates the conventional blind zone of atmospheric aerosol lidar systems within the initial hundred meters. Thirdly, SR-EBL offers higher spatial and temporal resolution than other lidar sensors, enabling more precise characterization of nvPM distributions, which is critical for assessing soot emissions in a complex environment such as an airport with multiple sources of pollution. Finally, the sensitivity of SR-EBL means that all particles can be detected over the entire lidar field of view in the vicinity of aircraft plumes. The ranging capability of the SR-EBL technique ensures that all particles are actually detected and not missed, as is the case with other local in situ techniques that rely on a complex sampling apparatus.

The original feature of this technique is that it can be operated directly out of the exhaust, without contact, and without sampling or diluting the soot particles in cells. The CAL sensor has been tested during a field campaign using a turbulent kerosene Jet A-1 pool-fire and has shown promising results for measuring nvPM concentrations in real-time. The next step here was to demonstrate the use of the CAL sensor in an airport campaign to assess its performance in a real-world scenario,

https://doi.org/10.5194/egusphere-2025-2612
Preprint. Discussion started: 7 August 2025

using a commercial aircraft engine. The results of this study provide valuable information about the potential use of the CAL sensor to assess the nvPM mass and number concentration in the vicinity of aircraft plumes.

3 Results

The objective here is to demonstrate the feasibility of remotely measuring PM emissions using the CAL sensor based on engine thrust conditions. A brief measurement campaign was conducted, as detailed in the following sections, to evaluate the potential use of the CAL sensor for measuring nvPM emissions of aircraft engines, both in terms of mass and number concentrations. This campaign aimed to further assess the performance and suitability of the sensor under real-world conditions on an airport. The data collected during this study provide valuable insights into the future capabilities of the CAL sensor for accurately characterizing aircraft nvPM emissions.

3.1 Experimental conditions

The measurements presented in this study were collected during an experimental campaign that was conducted in February 2022 at the Airbus SAS Bikini outdoor test facility, Toulouse Blagnac Airport (IATA:TLS), France (43°38′06″N, 1°22′04″E). The CAL sensor was easy and practical to operate for several hours at an airport. It was placed at a lateral distance of about 50 meters from the plume. Lidar measurements were conducted along a near-horizontal trajectory using the CAL sensor positioned inside a vehicle. The laser beam was maintained at an approximate height of 2 meters above the tarmac, precisely aligned to target and intersect the aircraft engine plume perpendicularly. A single Rolls-Royce Trent XWB-84 engine on an Airbus A350-900 Flight Lab aircraft was operated on conventional Jet A-1 fuel.

Figure 2. Picture of the test setup at the Airbus SAS Bikini outdoor test facility with an Airbus A350-900 Flight Lab test aircraft. The arrows indicate the location of the CAL sensor and a beam stop for laser safety.

https://doi.org/10.5194/egusphere-2025-2612
Preprint. Discussion started: 7 August 2025

3.2 Calibration

A significant challenge in conducting short-range lidar measurements is the incomplete overlap between the lidar's transmitter and receiver. This overlap issue is a primary cause of uncertainty when profiling the radiative and microphysical properties of aerosols using short-range lidars. This can be viewed as a variation in the image-plane position that depends on the range to the scattering volume, impacting the lidar's collection efficiency. Consequently, backscattered light in the short-range may not fully reach the optical sensor. This area is commonly known as the lidar incomplete overlap or blind zone. Despite numerous techniques proposed to determine the overlap function of lidar systems Halldórsson and Langerholc (1978); Harms (1979); Sasano et al. (1979); Dho et al. (1997); Wandinger and Ansmann (2002); Guerrero-Rascado et al. (2010); Vande Hey et al. (2011); Biavati et al. (2011); Li et al. (2016), experimental approaches are often preferred due to the lack of accurate lidar specifications required for theoretical methods. The CAL sensor features a bi-static, multi-axial design specifically aimed at profiling aerosols in the short-range while minimizing the incomplete overlap zone. A measurement of the range-dependent overlap function was performed using a Lambertian surface, as detailed in Ceolato et al. (2020a), to confirm that full overlap was achieved after 30 meters.

3.3 Aircraft PM measurements

In the following, the nvPM or equivalent black carbon (eBC) mass and number concentrations are derived from volume backscatter coefficients measured by our CAL sensor. Such backscatter measurements can be converted to mass concentrations by dividing them by a reference mass backscatter coefficient (MBC; units of $\mathrm{m^2 g^{-1} sr^{-1}}$) and number concentrations by dividing them by a reference differential backscatter cross-section ($\mathrm{d}C^{\mathrm{bac}}$; units of $\mathrm{m^2 g^{-1} sr^{-1}}$), following Eqs. 2.1 and 2.1 respectively. This data processing is similar to the one commonly used in optical techniques such as LII, CAPS, or PAX and also rely on a reference coefficient, although here the measurand is not incandescence or absorption but backscattering. The reference MBC used here to report eBC represents an assumed physical property of the nvPM emitted by the engine at a given time. In this study, we have used the value of $\mathrm{MBC} = 0.025\ \mathrm{m^2 g^{-1} sr^{-1}}$ and $\mathrm{d}C^{\mathrm{bac}} = 1.38\ \mathrm{nm^2 sr^{-1}}$, which is provided by the backscattering RDG-FA model, described in Section 2.2.

A series of lidar measurements were performed during the test under various engine thrust conditions. An adaptive gain system was employed to prevent saturation of the CAL sensor from ambient light while maximizing the signal-to-noise ratio. The recorded lidar signals were background-corrected and time-averaged to produce raw lidar signals. The volume backscatter profiles were then derived from these raw signals using the analysis methodology outlined in Section 2.1.

Figure 3 presents a time-range false-color map of the volume backscatter coefficient (left) from an initial measurement test and the retrieved nvPM mass and number concentration profiles (right). The left panel reveals temporal and spatial variations in backscattering, with a distinctly high backscatter coefficient at the location of the engine exhaust location. In particular, eBC particles are clearly detected from the background aerosols with a volume backscatter coefficient greater than $10^{-6}\ \mathrm{m^{-1} sr^{-1}}$. The right panel shows the time-integrated horizontal distributions of eBC mass and number concentrations, peaking at the engine location and forming an almost perfect Gaussian plume of about 6 meters. The presence of a crosswind during the

https://doi.org/10.5194/egusphere-2025-2612
Preprint. Discussion started: 7 August 2025

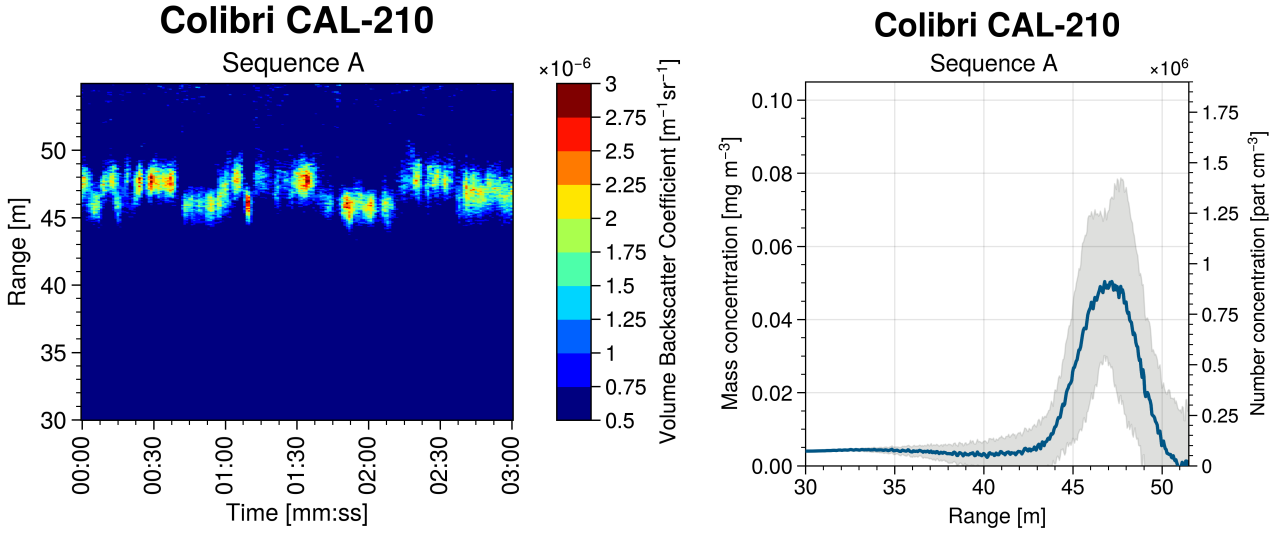

Figure 3. Time-range map of the volume backscatter coefficient (left). Retrieved equivalent black carbon mass and number concentration profiles.

measurement caused fluctuations in the volume backscatter profiles during the measurements. However, these instabilities were identified and found to have minimal effect on the results, as detailed in the mass and number concentration retrievals.

Figure 4 complements the previous analysis by illustrating a time-range map of the volume backscatter coefficient (top panel) and the retrieved nvPM mass and number concentration profiles (bottom panel) under three engine thrust conditions : intermediate, high, and ground idle. It is important to note that the measurement duration at high power was relatively brief compared to the longer periods recorded at intermediate power and idle power. The maximum mean and standard deviation values are reported in Table 2 for nvPM mass and number concentration. This result provides valuable insights into the temporal and spatial variations of nvPM emissions, with the CAL sensor effectively quantifying the changes in number and mass concentration corresponding to various engine thrust levels. Table 2 presents a comprehensive summary of the nvPM mass and number concentrations using the CAL sensor. It demonstrates a clear correlation between engine power and particulate emissions. The observed tendencies align with trends reported in the ICAO Aircraft Engine Emissions Databank International Civil Aviation Organization (2025), showing a non-linear relationship between engine thrust and emission levels: intermediate thrust produces the highest concentrations, followed by slightly lower values at high thrust, while idle conditions exhibit the lowest emissions. Interestingly, the concentrations do not increase linearly with thrust, suggesting complex interactions between engine parameters and particulate formation. These findings underscore the importance of considering specific engine operating conditions when assessing aircraft particulate emissions and their potential environmental impact.

https://doi.org/10.5194/egusphere-2025-2612
Preprint. Discussion started: 7 August 2025

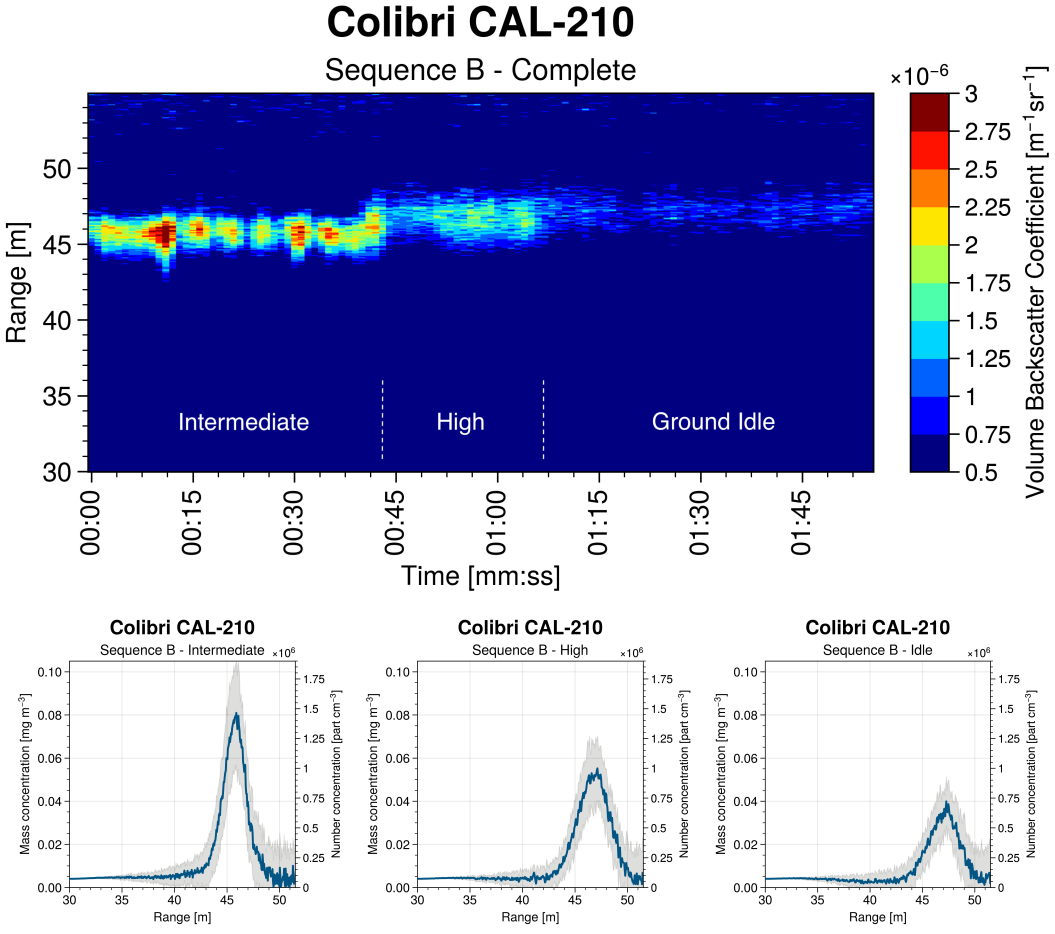

Figure 4. Time-range map of the volume backscatter coefficient (top) and retrieved equivalent black carbon mass and number concentration profiles (bottom) under three engine thrust conditions: intermediate, high, and idle.

Table 1. Mass and number concentrations obtained from the CAL sensor at various engine thrust conditions. Maximum and standard deviation values.

Engine thrust	Mass [mg m^{-3}]	Number [10^6 part cm^{-3}]
Intermediate	0.081 ± 0.018	1.47 ± 0.33
High	0.055 ± 0.014	0.99 ± 0.25
Idle	0.040 ± 0.009	0.72 ± 0.16

https://doi.org/10.5194/egusphere-2025-2612
Preprint. Discussion started: 7 August 2025

4 Discussion

New scientific instruments are urgently needed to quantify non-CO2 emissions (such as nvPM or contrails), which create complex climate impacts that cannot be addressed by traditional characterization methods alone. We propose to discuss several uncertainties and limitations, as well as potential developments to enhance the performance of the CAL sensor.

4.1 Uncertainties and limitations

Assessing uncertainties is a critical part in the development of any novel measurement method. Our analysis of the retrieval method reveals that one of the primary sources of uncertainty lies in the limited knowledge of the backscattering properties of particulate matter (PM) emitted by aircraft. To address this, an aerosol-optics model was introduced in Section 2.2, based on the following key equations:

$$\mathrm{d}C^{\mathrm{bac}} = 9\pi^2 \frac{V_{\mathrm{agg}}^2}{\lambda^4} F(m) S(q_\pi), \tag{13}$$

$$\mathrm{MBC} = \frac{\mathrm{d}C_{\mathrm{agg}}^{\mathrm{bac}}}{\rho V_{\mathrm{agg}}} = 9\pi^2 \frac{V_{\mathrm{agg}}}{\rho \lambda^4} F(m) S(q_\pi). \tag{14}$$

In light-scattering models, uncertainties in optical properties (e.g. refractive index) and morphological characteristics (e.g. fractal dimension, ratio of monomer radius to radius of gyration) can introduce substantial errors in the predicted backscattering behavior. To quantify the impact of these uncertainties on backscattering properties, we employ a Monte Carlo (MC) uncertainty analysis. This method involves generating a large number of random samples from the probability distributions of the input parameters, as summarized in Table 2, and evaluating the measurement model for each sample set. The resulting distribution of output values enables the estimation of both the best value and its associated uncertainty.

Table 2. Uncertainty components associated with optical properties and morphological properties of the backscattering model.

Components	Symbols	Units	Value	Uncertainty	Cback (% Var)	MBC (% Var)
Fractal dimension	D_f		1.9	± 0.1	6.8	6.2
Fractal pre-factor	k_f		2.3	± 0.2	6.3	5.7
$D_\mathrm{m}/D_\mathrm{g}$	X_R		0.40	± 0.02	7.3	6.7
Monomer radius	$\mathrm{R_m}$	nm	10.0	± 1	76.2	69.3
Scattering function	F(m)		0.4	± 0.05	3.4	12.4
Backscattering Structure Factor	$\mathrm{S}(q_\pi)$		0.89	± 0.01	0.0	0.1
Effective mass density	ρ	$\mathrm{kg\,m^{-3}}$	1000	± 0.100	N/A	0.0

A sensitivity analysis is presented in Fig. 5, with results for C^{bac} shown in the top panel and for MBC in the bottom. The analysis follows a one-at-a-time (OAT) approach, using Pearson correlation coefficients to quantify the influence of each input variable across the full ensemble of simulations. The scatter plots include linear regression fits, with the quality of the fit

https://doi.org/10.5194/egusphere-2025-2612
Preprint. Discussion started: 7 August 2025

assessed using the Root Mean Squared Error (RMSE) and the coefficient of determination (R^2). The R^2 values indicate that the investigated parameters have a substantial and variable impact on both C^{bac} and MBC, with explained variances of 78

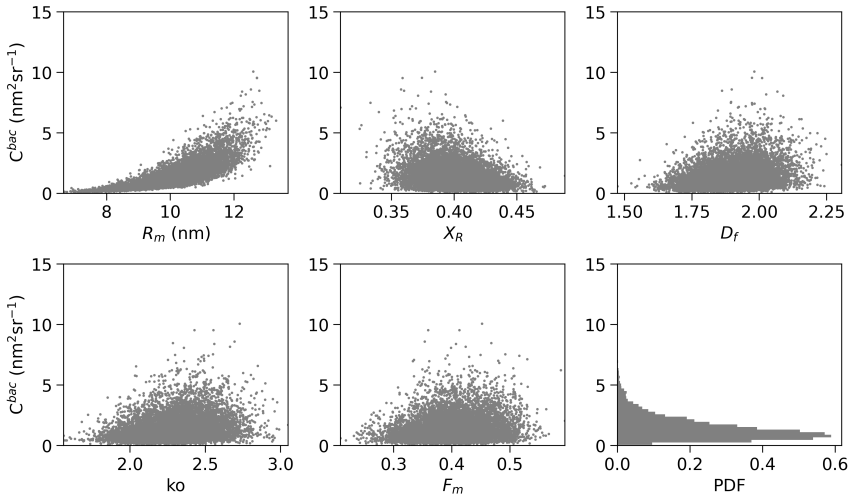

(a) Sensitivity analysis of C^{bac} with respect to key input parameters.

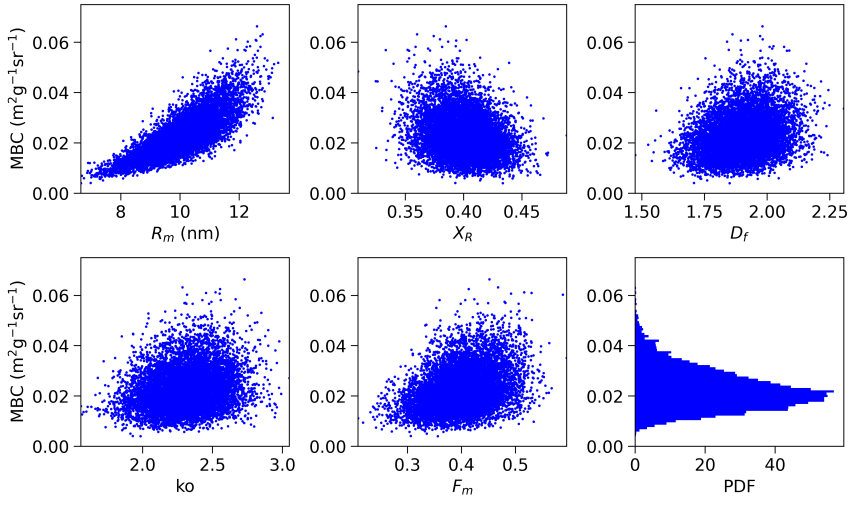

(b) Sensitivity analysis of MBC with respect to key input parameters.

Figure 5. The results of the sensitivity analysis, based on 10000 Monte Carlo simulations, are displayed. Each panel illustrates how individual parameters affect the variability of C^{bac} and MBC. The power density functions (PDFs) for C^{bac} and MBC are shown in the final figure of each panel.

The other variables that showed a moderate positive linear correlation, with R^2 values around 25%, are Df and k0 for both C^{bac} and MBC, while the only variable that exhibited an anti-correlation trend is X_R, with R^2 = 26%. Lastly, F(m) exhibits

https://doi.org/10.5194/egusphere-2025-2612
Preprint. Discussion started: 7 August 2025

a weaker but still notable linear influence on both MBC and C^{bac}, although the magnitudes differ. The linear relationship between MBC and F(m) accounts for a moderate R^2 of 33%, whereas the relationship between C^{bac} and F(m) is substantially weaker, with an R^2 of only 16%. This indicates that while both parameters show some positive linear correlation with F(m), MBC is more sensitive to variations in F(m) than C^{bac}. In contrast, S(qπ) exhibits a negligible linear correlation with both MBC and C^{bac}. This indicates that linear changes in S(qπ) do not significantly impact C^{bac} or MBC within the context of this analysis. It is important to note that this evaluation is based exclusively on linear regression. Therefore, depending on the analytical expression for S(q_π) presented in Eq. 11, additional nonlinear relationships may emerge, suggesting that new possible nonlinearities might exist beyond the scope of this linear analysis.

Based on the input data summarized in Table 2, the results of the Monte Carlo (MC) simulation — performed with 10,000 samples drawn from normal distributions—yield a mean value of $C^{\mathrm{bac}} = 1.4 \pm 1\,\mathrm{nm^2\,sr^{-1}}$, and a mean mass branching coefficient (MBC) of $(2.1 \pm 0.8) \times 10^{-2}\,\mathrm{m^2\,g^{-1}\,sr^{-1}}$. The distributions of these outputs are depicted in the histograms shown in Fig. 5. As expected, the probability density functions (PDFs) are normalized such that the area under each curve equals one. As observed, Eqs. 13 and 14 exhibit nonlinearities; therefore, the individual impact of each variable on the properties of interest cannot be fully captured through linear trends alone.

To evaluate the contribution of each variable, we expressed Equation 13 in logarithmic form and then quantified the variance associated with each term as follows:

$$\log C^{\mathrm{bac}} = \log A + 2\log V_{\mathrm{agg}} + \log S(q_\pi) + \log F_m \tag{15}$$

Operating with Eqs.8 and 9 the following explicit form of V_{agg} is used

$$V_{\mathrm{agg}} = \frac{4}{3}\pi\, k_0\, R_{\mathrm{m}}^3 \left(X_R^{-1}\right)^{D_f} \tag{16}$$

So Eq.16 it can be reformulated by combining the resulting terms as,

$$\log C^{\mathrm{bac}} = \log A + 2\left(\log k_o + 3\log R_{\mathrm{m}} + D_f \log\left(X_R^{-1}\right)\right) + \log S(q_\pi) + \log F_m. \tag{17}$$

Similarly for MBC, the Eq. 14 is decomposed as,

$$\log \mathrm{MBC} = \log k_o + 3\log R_{\mathrm{m}} + D_f \log\left(X_R^{-1}\right) + \log S(q_\pi) + \log F_m - \log\rho + \mathrm{B}. \tag{18}$$

where the $A = 9\pi^2/\lambda^4$ and B accounts for the unit conversion of MBC.

The results of the variable apportionment are summarized in the last two columns of Table 2. In a nutshell, R_m is the most influential variable for C_{bac}, accounting for up to 76.2% of the explained variance, and 69.3% in the case of MBC. The contributions from all other variables remain below 13% for both C_{bac} and MBC. This analysis further reveals that the variance of V_{agg} explains up to 96.6% of the variability in C_{bac}, and 87.9% in MBC.

https://doi.org/10.5194/egusphere-2025-2612
Preprint. Discussion started: 7 August 2025

4.2 Further development

This study introduces the CAL sensor, which was successfully used to measure nvPM emissions from the exhaust of an Airbus A350-900 Flight Lab aircraft engine. The sensor demonstrated high proficiency in real-time monitoring, providing critical insights into soot properties and behavior under varying engine conditions. The results confirmed the accurate assessment of nvPM equivalent mass and number concentrations, validating the CAL sensor's capability for characterizing aircraft exhaust. These findings highlight the potential of the CAL sensor to advance aerosol science, atmospheric research, and emission monitoring in the aviation sector, offering novel opportunities for improving regulatory compliance and environmental impact assessments.

Compared to the concentrations reported by ICAO, we are reasonably confident that the measurement uncertainties in our dataset are minimal. This supports the reliability of the aerosol optical model used to characterize aircraft PM emissions. This gives us confidence in the model's ability to reproduce key optical properties under realistic engine operating conditions. However, comparing emissions data from different measurement platforms is challenging due to the variability introduced by particle dilution in the engine exhaust plume. The dilution factor, which is governed by ambient conditions, distance from the exhaust, and plume mixing dynamics, can substantially alter the observed particle concentration. Further work should include a direct comparison between in-situ measurements obtained near the engine exit plane and remote-sensing observations, such as lidar measurements taken further downwind. Accurately accounting for dilution is essential to ensure meaningful comparisons and model validation across different spatial and temporal measurement regimes.

Future research should also address the formation and evolution of vPM. Lidar techniques offer the unique capability to sample exhaust plumes both near the emission source, at the engine exit plane, and at greater distances where vPM may form through cooling and condensation processes. This capability could improve upon traditional in-situ sampling methods and provide a more comprehensive assessment of total particulate matter (tPM), which includes both nvPM and vPM. Another key challenge is assessing particulate matter emission indices from lidar measurements by integrating engine performance data, such as fuel flow rates or carbon dioxide concentrations, in accordance with ICAO emission-index standards. This represents a future critical step toward standardized quantification of aircraft emissions.

5 Conclusion

We developed and deployed a short-range elastic backscatter lidar, named CAL sensor, to measure the PM emissions of aircraft engine on an airport in Toulouse. Field results demonstrate that the CAL sensor can reliably measure backscatter profiles of PM emitted by the engine at various thrust levels. By applying a backscattering model for soot particles, CAL sensor measurements can be inverted to determine both number and mass concentrations. Utilizing CAS sensor capabilities could enhance the quantification of PM emissions. Using the capabilities of CAS sensors could help to better quantify PM emissions. Overall, our findings support further development of the CAL sensor as a flexible solution to quantify aircraft PM emissions.

This work presents a novel, non-invasive method for measuring particulate matter (PM) emissions from aircraft engines using a compact, field-deployable lidar system. This technology enables real-time, remote assessment of PM emissions at airports,

https://doi.org/10.5194/egusphere-2025-2612
Preprint. Discussion started: 7 August 2025

addressing a major challenge in air quality monitoring and regulatory compliance. Aircraft engine PM emissions are a pressing environmental and public health concern due to their role in degrading air quality around airports and their contribution to contrail formation, which impacts climate. Our approach provides a breakthrough by allowing rapid and accurate emission measurements without the need for direct sampling, which is logistically complex and often impractical. This advancement is timely and relevant, as it supports efforts to reduce aviation's environmental footprint and informs policy on sustainable air transport. The research is particularly newsworthy because it introduces a new measurement capability with direct implications for air quality management, climate research, and regulatory monitoring. Such topics are believed to be of high public and media interest. The method's successful demonstration at a major European test site further enhances its relevance and potential for broad application. In a nutshell, our findings offer a significant step forward in environmental monitoring technology, with clear benefits for science, policy, and society.

Author contributions. RC developed the instrument and the methodology, with support from AB, GL, LG, AV, IO, and DD. The date were analyzed and processed by AB and RC. RC drafted the manuscript, with contributions and revisions from AB and CR. The experimental trials were initiated and coordinated by PL, CR, KS, and MJ. The structure and scope of the paper were defined collaboratively by all the authors.

Competing interests. The contact author has declared that none of the authors has any competing interests.

Acknowledgements. The authors express their sincere gratitude to the individuals and organizations whose contributions were invaluable to this research. We thank Prof. Jerome Yon, Prof. Matthew J. Berg, and Prof. Chris Sorensen for their expert advice on soot characterization and light-scattering models. Our appreciation extends to the Airbus Flight-Lab team for their support in conducting lidar measurements and providing access to test facilities. We are grateful to Gauthier Le Chenadec, Maxime Gauthier, and Abhijeet Sanjay Badhe for their assistance and contributions. The ongoing development, production, assessment, and analysis of CAL instrument and data are supported by ONERA. We acknowledge the Direction Générale de l'Aviation Civile (DGAC), ONERA's Direction Scientifique Générale (DSG), and Direction Programme Aéronautique (DPA) for their scientific guidance and resources that were crucial for this research. This work would not have been possible without their collective expertise and support.

https://doi.org/10.5194/egusphere-2025-2612
Preprint. Discussion started: 7 August 2025

References

Bedoya-Velásquez, A. E., Ceolato, R., Titos, G., Bravo-Aranda, J. A., Casans, A., Patrón, D., Fernández-Carvelo, S., Guerrero-Rascado, J. L., and Alados-Arboledas, L.: Synergy between Short-Range Lidar and In Situ Instruments for Determining the Atmospheric Boundary Layer Lidar Ratio, Remote Sensing, 16, https://doi.org/10.3390/rs16091583, 2024.

Biavati, G., Di Donfrancesco, G., Cairo, F., and Feist, D. G.: Correction scheme for close-range lidar returns, Appl Opt, 50, 5872–82, https://doi.org/10.1364/AO.50.005872, 2011.

Ceolato, R. and Berg, M. J.: Aerosol light extinction and backscattering: A review with a lidar perspective, Journal of Quantitative Spectroscopy and Radiative Transfer, 262, 107 492, https://doi.org/https://doi.org/10.1016/j.jqsrt.2020.107492, 2021.

Ceolato, R., Bedoya-Velásquez, A. E., and Mouysset, V.: Short-Range Elastic Backscatter Micro-Lidar for Quantitative Aerosol Profiling with High Range and Temporal Resolution, Remote Sensing, 12, https://doi.org/10.3390/rs12203286, 2020a.

Ceolato, R., Bedoya-Velásquez, A. E., and Mouysset, V.: Short-Range Elastic Backscatter Micro-Lidar for Quantitative Aerosol Profiling with High Range and Temporal Resolution, Remote Sensing, 12, https://doi.org/10.3390/rs12203286, 2020b.

Ceolato, R., Bedoya-Velasquez, A., Fossard, F., Mouysset, V., Paulien, L., Lefebvre, S., Mazzoleni, C., Sorensen, C., Berg, M., and Yon, J.: Black carbon aerosol number and mass concentration measurements by picosecond short-range elastic backscatter lidar, Scientific Reports, 12, 8443, https://doi.org/10.1038/s41598-022-11954-7, 2022.

Delhaye, D., Ouf, F.-X., Ferry, D., Ortega, I. K., Penanhoat, O., Peillon, S., Salm, F., Vancassel, X., Focsa, C., Irimiea, C., Harivel, N., Perez, B., Quinton, E., Yon, J., and Gaffie, D.: The MERMOSE project: Characterization of particulate matter emissions of a commercial aircraft engine, Journal of Aerosol Science, 105, 48–63, https://doi.org/https://doi.org/10.1016/j.jaerosci.2016.11.018, 2017.

Dho, S. W., Park, Y. J., and Kong, H. J.: Experimental determination of a geometric form factor in a lidar equation for an inhomogeneous atmosphere, Applied Optics, 36, https://doi.org/10.1364/ao.36.006009, 1997.

Digby, R. A. R., von Salzen, K., Monahan, A. H., Gillett, N. P., and Li, J.: The impact of uncertainty in black carbon's refractive index on simulated optical depth and radiative forcing, EGUsphere, 2024, 1–27, https://doi.org/10.5194/egusphere-2024-1796, 2024.

Durand, E., Durdina, L., Smallwood, G., Johnson, M., Spirig, C., Edebeli, J., Roth, M., Brem, B., Sevcenco, Y., and Crayford, A.: Correction for particle loss in a regulatory aviation nvPM emissions system using measured particle size, Journal of Aerosol Science, 169, 106 140, https://doi.org/https://doi.org/10.1016/j.jaerosci.2023.106140, 2023.

Durdina, L., Brem, B., Abegglen, M., Lobo, P., Rindlisbacher, T., Thomson, K., Smallwood, G., Hagen, D., Sierau, B., and Wang, J.: Determination of PM mass emissions from an aircraft turbine engine using particle effective density, Atmospheric Environment, 99, 500–507, https://doi.org/https://doi.org/10.1016/j.atmosenv.2014.10.018, 2014.

Fengshan Liu, Jérôme Yon, A. F. P. L. G. J. S. and Corbin, J. C.: Review of recent literature on the light absorption properties of black carbon: Refractive index, mass absorption cross section, and absorption function, Aerosol Science and Technology, 54, 33–51, https://doi.org/10.1080/02786826.2019.1676878, 2020.

Guerrero-Rascado, J. L., ao Costa, M. J., Bortoli, D., Silva, A. M., Lyamani, H., and Alados-Arboledas, L.: Infrared lidar overlap function: an experimental determination, Opt. Express, 18, 20 350–20 369, https://doi.org/10.1364/OE.18.020350, 2010.

Halldórsson, T. and Langerholc, J.: Geometrical form factors for the lidar function, Applied Optics, 17, https://doi.org/10.1364/ao.17.000240, 1978.

Harms, J.: Lidar return signals for coaxial and noncoaxial systems with central obstruction, Appl Opt, 18, 1559–66, https://doi.org/10.1364/AO.18.001559, 1979.

https://doi.org/10.5194/egusphere-2025-2612
Preprint. Discussion started: 7 August 2025

ICAO: Annex 16 to the Convention on International Civil Aviation: Environmental Protection, Volume II — Aircraft Engine Emissions, ICAO, 4th edn., 2017.

ICAO: International Standards and Recommended Practices, Environmental Protection, Volume II: Aircraft Engine Emissions, Tech. rep., International Civil Aviation Organization, Montréal, Canada, amendment 9, plus further amendments: Amendment 10, effective 1 January 2021, 2017.

International Civil Aviation Organization: ICAO Aircraft Engine Emissions Databank, https://www.easa.europa.eu/en/domains/environment/icao-aircraft-engine-emissions-databank, accessed: Feb. 1, 2025, 2025.

Ishimoto, H., Kudo, R., and Adachi, K.: A shape model of internally mixed soot particles derived from artificial surface tension, Atmospheric Measurement Techniques, 12, 107–118, https://doi.org/10.5194/amt-12-107-2019, 2019.

Jones, S. H. and Miake-Lye, R. C.: Parameterization of H2SO4 and organic contributions to volatile PM in aircraft plumes at ground idle, Journal of the Air & Waste Management Association, 74, 490–510, https://doi.org/10.1080/10962247.2024.2354820, 2024.

Kanngiesser, F. and Kahnert, M.: Coating material-dependent differences in modelled lidar-measurable quantities for heavily coated soot particles, Opt. Express, 27, 36 368–36 387, https://doi.org/10.1364/OE.27.036368, 2019.

Klöwer, M., Allen, M. R., Lee, D. S., Proud, S. R., Gallagher, L., and Skowron, A.: Quantifying aviation's contribution to global warming, Environmental Research Letters, 16, 104 027, https://doi.org/10.1088/1748-9326/ac286e, 2021.

Kumal, R. R., Liu, J., Gharpure, A., Vander Wal, R. L., Kinsey, J. S., Giannelli, B., Stevens, J., Leggett, C., Howard, R., Forde, M., Zelenyuk, A., Suski, K., Payne, G., Manin, J., Bachalo, W., Frazee, R., Onasch, T. B., Freedman, A., Kittelson, D. B., and Swanson, J. J.: Impact of Biofuel Blends on Black Carbon Emissions from a Gas Turbine Engine, Energy & Fuels, 34, 4958–4966, https://doi.org/10.1021/acs.energyfuels.0c00094, 2020.

Lee, D. S., Allen, M. R., Cumpsty, N., Owen, B., Shine, K. P., and Skowron, A.: Uncertainties in mitigating aviation non-CO2 emissions for climate and air quality using hydrocarbon fuels, Environ. Sci.: Atmos., 3, 1693–1740, https://doi.org/10.1039/D3EA00091E, 2023.

Li, J., Li, C., Zhao, Y., Li, J., and Chu, Y.: Geometrical constraint experimental determination of Raman lidar overlap profile, Appl Opt, 55, 4924–8, https://doi.org/10.1364/AO.55.004924, 2016.

Liu, L. and Mishchenko, M. I.: Spectrally dependent linear depolarization and lidar ratios for nonspherical smoke aerosols, Journal of Quantitative Spectroscopy and Radiative Transfer, 248, 106 953, https://doi.org/https://doi.org/10.1016/j.jqsrt.2020.106953, 2020.

Marhaba, I., Ferry, D., Laffon, C., Regier, T. Z., Ouf, F.-X., and Parent, P.: Aircraft and MiniCAST soot at the nanoscale, Combustion and Flame, 204, 278–289, https://doi.org/https://doi.org/10.1016/j.combustflame.2019.03.018, 2019.

Measures, R. M.: Laser remote sensing: Fundamentals and applications, New York, Wiley-Interscience, 1984.

Mishchenko, M. I., Travis, L. D., and Lacis, A. A.: Scattering, absorption, and emission of light by small particles, Cambridge university press, 2002.

N. Moteki, Sho Ohata, A. Y. and Adachi, K.: Constraining the complex refractive index of black carbon particles using the complex forward-scattering amplitude, Aerosol Science and Technology, 57, 678–699, https://doi.org/10.1080/02786826.2023.2202243, 2023.

Qin, Z., Wang, H., He, A., Sun, Y., Li, J., Zhang, Y., and Zhang, Q.: Backscattering Linear Depolarization Ratio of Smoke Aerosols From Biomass Burning, Journal of Geophysical Research: Atmospheres, 129, e2024JD041 276, https://doi.org/https://doi.org/10.1029/2024JD041276, e2024JD041276 2024JD041276, 2024.

SAE International: Procedure for the Continuous Sampling and Measurement of Non-Volatile Particulate Matter Emissions from Aircraft Turbine Engines, Aerospace Recommended Practice ARP6320, SAE International, 2018.

https://doi.org/10.5194/egusphere-2025-2612
Preprint. Discussion started: 7 August 2025

SAE International: Procedure for the Calculation of Non-Volatile Particulate Matter Sampling and Measurement System Losses and System Loss Correction Factors, Aerospace Recommended Practice ARP6481, SAE International, 2019.

Sasano, Y., Shimizu, H., Takeuchi, N., and Okuda, M.: Geometrical form factor in the laser radar equation: an experimental determination, Appl Opt, 18, 3908–10, https://doi.org/10.1364/AO.18.003908, 1979.

Smith, A. J. A., Peters, D. M., McPheat, R., Lukanihins, S., and Grainger, R. G.: Measuring black carbon spectral extinction in the visible and infrared, Journal of Geophysical Research: Atmospheres, 120, 9670–9683, https://doi.org/https://doi.org/10.1002/2015JD023564, 2015.

Sorensen, C. M.: Light Scattering by Fractal Aggregates: A Review, Aerosol Science and Technology, 35, 648–687, https://doi.org/10.1080/02786820117868, 2001.

Teoh, R., Stettler, M. E., Majumdar, A., Schumann, U., Graves, B., and Boies, A. M.: A methodology to relate black carbon particle number and mass emissions, Journal of Aerosol Science, 132, 44–59, https://doi.org/https://doi.org/10.1016/j.jaerosci.2019.03.006, 2019.

U. Trivanovic, G. A. K. and Pratsinis, S. E.: High-throughput generation of aircraft-like soot, Aerosol Science and Technology, 56, 732–743, https://doi.org/10.1080/02786826.2022.2070055, 2022.

Vande Hey, J., Coupland, J., Foo, M. H., Richards, J., and Sandford, A.: Determination of overlap in lidar systems, Appl Opt, 50, 5791–7, https://doi.org/10.1364/AO.50.005791, 2011.

Wandinger, U. and Ansmann, A.: Experimental determination of the lidar overlap profile with Raman lidar, Applied Optics, 41, https://doi.org/10.1364/ao.41.000511, 2002.

Yu, F., Kärcher, B., and Anderson, B. E.: Revisiting Contrail Ice Formation: Impact of Primary Soot Particle Sizes and Contribution of Volatile Particles, Environmental Science & Technology, 58, 17 650–17 660, https://doi.org/10.1021/acs.est.4c04340, pMID: 39323293, 2024.